Wash waves generated by ship moving across a depth change

Mingxin Li [a], Zhi-Ming Yuan [b,*], Longbin Tao [a,b]

[a] *School of Naval Architecture and Ocean Engineering, Jiangsu University of Science and Technology, Zhenjiang, China*
[b] *Department of Naval Architecture, Ocean & Marine Engineering, University of Strathclyde, UK*

ARTICLE INFO

ABSTRACT

Unsteady wash waves generated by a ship with constant speed moving across an uneven bottom topography is investigated by numerical simulations based on a Mixed Euler–Lagrange (MEL) method. The transition is accomplished by the ship traveling from the deep water into shallow water via a step bottom. A small tsunami would be created after this transition. However, the unsteady wave-making resistance induced by this new phenomenon has not been well documented by literature. Therefore, the main purpose of the present study is to quantify the effects of an uneven bottom on the unsteady wash waves and wave-making resistance acting on the ship. An upwind differential scheme is commonly used in the Euler method to deal with the convection terms on free-surface condition to prevent waves in upstream. Evidently, it cannot be applied to the present problem when the ship-generated waves could propagate upstream. A MEL method is therefore employed to investigate the upstream wave generated by the ship moving over the uneven bottom. The central differential scheme provides more accurate results, but it is not unconditionally stable. Simulation results show that the hydrodynamic interaction between the ship and the uneven bottom could initiate an upstream tsunami, as well as unsteady wave-making resistance on ships. The unsteady wave-making resistance oscillates periodically, and the amplitude and period of the oscillations are highly dependent on speed and water depth.

1. Introduction

Although ships spend the majority of their operational time sailing at waterways of uniform depth, the unsteady effects can be important in some circumstances. In practical operations, when a ship maneuvers in a port/harbour/lock environment, a ship is likely to travel in close proximity to waterway boundaries with an abrupt change, i.e., in bank dimension or bottom depth; during ship model testing, a false bottom has been installed to mimic the change in the water depth in an 'idealistic' approach (Li et al., 2020b). The false bottom usually does not cover the full length of the towing tank. Therefore, as a ship model manoeuvres from deep water to finite-depth water, unsteady effects are experienced. Under these circumstances, the upstream waves could be generated by a ship in a steady motion over the uneven bottom (Grue, 2020), and the wave resistance forced on the ship could not maintain a steady value. However, the unsteady wash wave problem of the hydrodynamic interaction between the ship and the uneven bottom has received only a limited amount of attention.

Pioneering studies have provided fundamental insight into the unsteady wave-making resistance as the most important hydrodynamic

performance of a ship. Lunde (1951) developed an unsteady theory to analyse the ship-wave problem. Based on Lunde's theory, Wehausen (1964) proposed asymptotic formulas to predict the unsteady wave resistance of a ship. The experiments conducted by Doctors et al. (2008) showed that the presented linearised theory provided excellent predictions of the acceleration effect on the resistance. The inland ships are most likely to manoeuvre in shallow water, which has a significant effect on the wave resistance. The behaviour of a ship in shallow water was investigated by slender-body theory (Chen and Sharma, 1995; Gourlay, 2008; Tuck, 1966) and experimental measurements (Kijima and Nakiri, 1990). Apart from the theory method or experiments, with the development of higher-performance computers, many numerical methods have been implemented to solve the shallow water problem. Terziev et al. (2020) and Shi et al. (2020) used the Computational Fluid Dynamics (CFD) software StarCCM + to study the hydrodynamic interaction between the hull and the uneven seabed. The former only examined the increased resistance encountered by a ship with transcritical speed; the latter does not predict the upstream wave and unsteady wave resistance. The CFD method is time costly and resource-consuming. Thus, the unsteady wave problem of ships in shallow water remains a

---

challenging issue. The shallow water equation has been used numerically to simulate the waves generated by a ship at critical speed in limited water depths. Torsvik et al. (2006) investigated the speed effects on the waves generated by a ship passing through the transcritical speed region in shallow water based on Boussinesq equations. In their simulations, they examined the amplitude of the waves generated by a ship with various transcritical speeds. However, the method of the shallow water equation has limitations in establishing complex models.

Li and Sclavounos (2002) used modified Boussinesq equations to calculate the nonlinear long waves generated by a disturbance moving at a critical speed. Jiang et al. (2002) combined extended Boussinesq equations for the far-field flow and slender-body theory for the near-ship flow. The wash waves generated by ships were investigated, considering varying topographies. Alam and Mei (2008) examined the ship-generated waves in a shallow channel with a randomly uneven bed when the ship speed is near-critical.

Based on the observed new phenomenon in the Oslofjord, Grue (2017) found that the very long waves are generated when a ship moves across an appreciable depth change with subcritical speed by asymptotic analysis. Then, theory and numerical calculations for a real ship geometry are compared with a moving pressure distribution and a few available wave height measurements (Grue, 2020). Wang and Cheng (2021) measured the long tsunami-like waves generated by cruise ships, suggested the fundamental similarity in the generation of tsunami as induced by mega-ships, landslides, or earthquakes as a process that causes vertical velocity at the sea surface. However, the unsteady wave resistance was not quantified within the ship's transition around uneven bottom. Apart from the simulation method finite element method (FEM) used in shallow water equation and finite volume method (FVM) used in CFD method, the boundary element method (BEM) has been widely applied on hydrodynamic performance simulation. BEM, based on the Green's theorem, has been a highly effective means of computing the linear/nonlinear free surface flow around arbitrary 3D bodies for a long time (Yeung, 1978, 1982; Yeung and Tan, 1980). Based on Hess and Smith (1964), who utilised a distribution of source density on the surfaces of the computational domain, Dawson (1977) initially introduced the Rankine panel method in a practical form to linearise the free surface condition. The major advantages of the Rankine singularities method include the simplicity of the source singularity and the potential of employing the nonlinear free surface condition (Raven, 1996). Some researchers investigated a ship moving from the rest to a constant speed in different water depths to predict the unsteady wave resistance (He et al., 2014; Kring, 1994; Nakos et al., 1994). Furthermore, unsteady waves generated between multiships were simulated by Rankine source method in the time domain (Yeung and Tan, 1980; Yuan et al., 2019) or based on the newly developed time-stepping algorithm (Li et al., 2021). The traditional Euler method and explicit Euler scheme have been investigated; they were unconditionally unstable and conditionally stable, respectively (Park and Troesch, 1993). To develop the stability and prevent an upstream wave ahead of the ship, the upwind scheme was adopted at the convection term of the free surface condition in the Euler method (Bunnik, 1999). These results were calculated based on the Euler method, which is inappropriate for the problem of the upstream wave in the present study. Therefore, the MEL method, which does not require the convection term, could be employed to investigate the upstream wave generated by the ship over an uneven bottom. Longuet-Higgins and Cokelet (1976) initially developed the MEL method for 2D free surface waves. Faltinsen (1977) applied the MEL method to compute the interaction of waves with a floating body. Following these pioneering works, variations of this approach have been applied to various body-wave problems, considering the nonlinear free surface (Cheng et al., 2022; Dommermuth et al., 1987; Jensen, 1986). Beck (1999b) reviewed the use of a desingularised Euler–Lagrange time stepping approach by the isolated Rankine source to solve fully nonlinear water wave problems. It proved that as an example of the application of the method to highly nonlinear shallow water waves, Cao

et al. (1993) predicted upstream runaway solitons in 2D by desingularised MEL method. Kara et al. (2007) solved free surface waves generated by Wigley and Series 60 hulls for the steady problem using a MEL method. Feng et al. (2010) calculated the wave-making resistance of the catamaran with a nonlinear wash wave in time domain by adopting the moving computational window based on the MEL method. These procedures are useful but limited in their range of application due to the flat bottom of deep or shallow water. Therefore, two major tasks are tested in the present study. Initially, the developed MEL method would be implemented into the program to study the upstream waves and unsteady wave resistance to be validated by comparing with other results. Then, the effect of the hydrodynamic between the ship and uneven bottom on the upstream wave and unsteady wave resistance would be quantified for analysis. This problem is solved in the time domain using the Rankine source method combined with the MEL method. The results are compared with the solutions of the upstream waves in Grue (2017). Finally, we provide a numerical analysis to investigate the upstream wave generation by the ship moving at subcritical speed across the depth changes and the oscillation characteristics of the unsteady wave resistance.

2. Numerical method

2.1. Governing equation and boundary conditions

The schematic of a single ship passing over the uneven bottom with constant velocity U is shown in Fig. 1, where the free surface S_f, the body surface S_b, the sidewall S_w and the bottom S_{bottom} are defined below. The transition is accomplished by the ship moving from the depth h_1 (deep water) over the depth h_2 (shallow water). Two right-handed coordinate systems are used: a global reference frame **o-$x_0 y_0 z_0$** fixed to the leading corner of the step bottom, and a local reference frame **o-xyz** fixed to the centre plane of the vessel with $z = 0$ at the free surface at rest.

Based on the assumption of ideal potential flow and the flow irrotational, the velocity potential $\varphi(x, y, z, t)$ satisfies the Laplace equation in the field, as follows:

$$\nabla^2 \varphi = 0 \tag{1}$$

The exact nonlinear kinematic and dynamic free surface boundary condition (FSBC) are as follows:

$$\frac{D\zeta}{Dt} = \frac{\partial \varphi}{\partial z} - \nabla\varphi \cdot \nabla\zeta \quad \text{on } z = \zeta \tag{2}$$

$$\frac{D\varphi}{Dt} = -g\zeta - \frac{1}{2}\nabla\varphi \cdot \nabla\varphi \quad \text{on } z = \zeta \tag{3}$$

where $\zeta(x, y, t)$ is the free surface elevation, and g is the gravitational acceleration, $D/D_t = \partial/\partial_t + \nabla\varphi \cdot \nabla$ is the substantial derivative following the fluid particle. The free surface condition is satisfied on the unknown surface $z = \zeta$. The non-piercing condition applied on the mean wetted surface of the body, as follows:

$$\frac{\partial \varphi}{\partial n} = U \cdot \vec{n} \tag{4}$$

and the non-piercing condition is applied on the water bottom, indicating the normal velocity at the bottom surface S_{bottom} is zero,

$$\frac{\partial \varphi}{\partial n} = 0 \tag{5}$$

The far-field condition ensures that the fluid disturbance must vanish at infinity,

$$\nabla\varphi \to 0 \text{ (as } \vec{x} \to \infty) \tag{6}$$

where $\vec{x} = (x, y, z)$ is the position vector of a fluid particle, and $\vec{n}$ is the unit normal vector of the body surface pointing into the fluid. In addi-
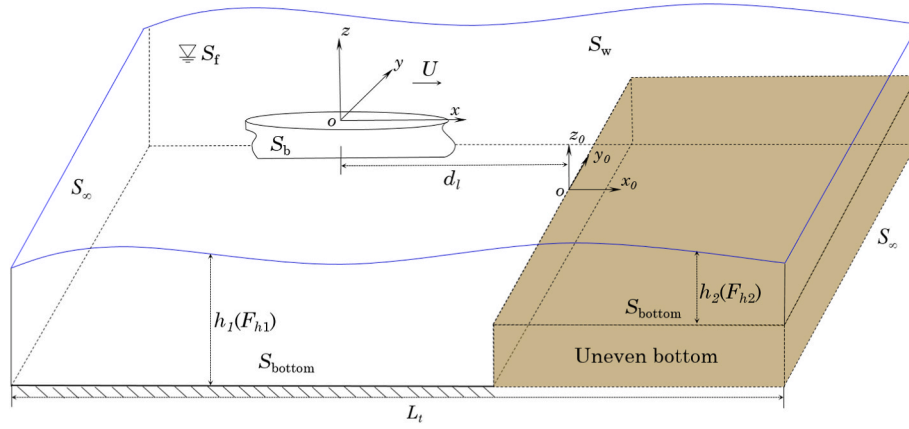
Fig. 1. Sketch of the problem and the definition of the coordinate systems.

tion, the initial value of the variables φ and ζ must be specified such that,

$$\begin{aligned} \varphi = 0 \quad (t \le 0) \\ \zeta = 0 \quad (t \le 0) \end{aligned} \text{ in the fluid domain} \tag{7}$$

The pressure on the body surface is given by Bernoulli's equation, as follows:

$$-p = \frac{\partial \varphi}{\partial t} + gz + \frac{1}{2}\nabla\varphi \cdot \nabla\varphi \quad = \frac{D\varphi}{Dt} + gz + \left(\frac{1}{2}\nabla\varphi - U\right) \cdot \nabla\varphi \tag{8}$$

This procedure is repeated as time proceeds. The forces and moments acting on the body are solved by integrating the pressure over the mean wetted surface, as follows:

$$\vec{F} = \iint_{Sb} -p\vec{n}ds \tag{9}$$

and

$$\vec{M} = \iint_{Sb} -p(\vec{r} \times \vec{n})ds \tag{10}$$

where $\vec{r}$ is the position vector of the body surface point to a reference point.

2.2. Solution procedure based on MEL method

The initial boundary value problems (1)–(6) for the body-wave problem over uneven bottom are solved using the MEL method with associated boundary conditions. During each time step, the solution procedure is divided into two parts: the Eulerian phase and the Lagrangian phase. The following boundary value problem with a Dirichlet condition on the free surface S_f and a Neumann condition on the body surface S_b is solved in the Eulerian frame at each time step, as follows:

$$\nabla^2 \varphi = 0, \text{ in the fluid domain } \Omega \tag{11}$$

$$\varphi = \varphi_0, \text{ in } S_f \tag{12}$$

$$\frac{\partial \varphi}{\partial n} = \vec{U} \cdot \vec{n}, \text{ in } S_b \tag{13}$$

$$\frac{\partial \varphi}{\partial n} = 0, \text{ in } S_{\text{bottom}} \tag{14}$$

$$\nabla\varphi \to 0, \text{ as } \vec{x} \to \infty \tag{15}$$

where φ_0 and $\vec{x}$ are known from the previous time step. After solving the boundary value problem, the velocities of the fluid particles con-

structing the FSBC can be calculated. In the Lagrangian phase, these velocities calculated in the Eulerian phase can be used to integrate the FSBC (2)–(3) with respect to the time required to advance the solution in the time domain. This fully nonlinear FSBC can be written in a new Lagrangian form, as follows:

$$\frac{D\vec{x}_f}{Dt} = \nabla\varphi + U\vec{i} \tag{16}$$

$$\frac{D\varphi}{Dt} = -gz - \frac{1}{2}\nabla\varphi \cdot \nabla\varphi \tag{17}$$

where $\vec{x}_f = (x, y, z)$ is the position vector of a fluid particle on the free surface, and $\vec{i}$ denotes the unit vector in the x-axis. The left-hand sides (LHS) of Eqs.16 and 17 are the derivatives of the potential and position of the moving particles with respect to time. On the right-hand side (RHS), all the quantities are known. Thus, the new potential φ and position $\vec{x}$ on the free surface can be easily determined based on the quantities φ_0 and $\vec{x}$ solved at the previous time step. The advantage of this MEL approach is that no other spatial derivative is required on the LHS, which reduces the numerical reflection from the truncated boundary (Kara et al., 2007). An effective time matching method of explicit fourth–order Runge–Kutta (RK4) is adopted in the Lagrangian phase for time-accurate calculations. For long-time simulation with a reasonable-sized fluid domain, the computational window scheme (Beck, 1999a) is used to maintain the computational domain during the simulation, as shown in Fig. 2. The position of the body within it is fixed because the computational window moves with the body. From the point of view of the body, the fluid particles have a tendency to drift
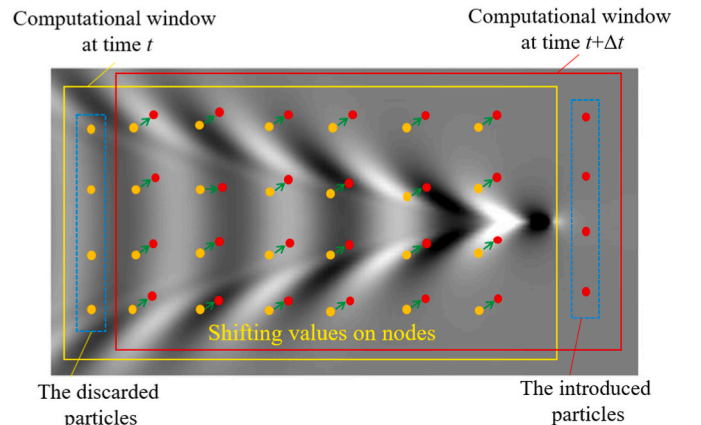

Fig. 2. Sketch of the shifting values on nodes in computational window.

downstream in the stream-wise direction. New particles with zero potential and elevation, $\varphi_{new} = \zeta_{new} = 0$, drift into the window upstream, whereas fluid particles drift out of the window downstream at each time step.

We specify the same number of fluid particles in and out based on the regridding scheme to maintain the same number of fluid particles in the computational window. At the end of each time step, the regridding technology should be implemented into the values of the free surface, including the elevation ζ, and the velocity potential φ would be interpolated into the original translating coordinate system with the same domain size using a cubic spline interpolation. This grid regeneration method is arranged on the free surface to determine the approximation of the actual free surface for the next time step. This process can be called node shifting (Tang, 2006). In fact, this process is consistent with the far-field boundary condition at the truncation boundary to be implemented into the node shifting scheme. For the surface-piercing problem, an intersection between the free surface and the body surface is found. The resolution of the panel vertices from both sides matches the intersection line, implying that panels connect on the intersection line.

2.3. Numerical method

To solve the boundary value problem for the disturbance velocity potential, constant-strength panels are employed on the S_f, S_b, and S_{bottom}. In terms of the Rankine source method, the potential at any point in the fluid domain is given by the following:

$$\varphi(\vec{x}) = \iint_S \sigma\left(\vec{x}_s\right) G\left(\vec{x}, \vec{x}_s\right) dS \qquad (18)$$

where S is the integration surface outside the fluid domain, the potential $\varphi(\vec{x})$ at the evaluation point $\vec{x}$, and $\sigma(\vec{x}_s)$ is an unknown source strength at the $\vec{x}_s$, which is denoted as the position vector on the boundary; the Rankine-type Green function satisfies the sea bed boundary condition at depth of h_1 through the method of mirror image, as follows:

$$G\left(\vec{x}, \vec{x}_s\right) = \frac{1}{\sqrt{\left|\vec{x} - \vec{x}_s\right|^2}} + \frac{1}{\sqrt{(x - x_s)^2 + (y - y_s)^2 + (z + 2h_1 + z_s)^2}} \qquad (19)$$

The Rankine sources are distributed above the integration surface to construct the velocity potential, and equation (18) reduces to a simple summation of the influence of each source, as follows:

$$\varphi(\vec{x}) = \sum_{j=1}^{N_F} \frac{\sigma_j^F}{\left|\vec{x} - \vec{x}_{s_j}^F\right|} + \sum_{j=1}^{N_B} \frac{\sigma_j^B}{\left|\vec{x} - \vec{x}_{s_j}^B\right|} \qquad (20)$$

where N_F is the number of the isolated sources above the free surface, $x_{s_j}^F$ is the location of the jth source, and σ_j^F is the strength of the jth source at $x_{s_j}^F$. Similarly, N_B, $x_{s_j}^B$ and σ_j^B are the number, location and strength of the sources distributed in the body surface. The integral Eqs. (12) and (13) are solved by discretisation of the integrals to form a system of linear equations. The detailed approach presented here can be determined in the same way by Hess and Smith (1964).

3. Numerical results

3.1. Convergence and validation tests

We initially consider the convergence test of the accelerating point source under the free surface. The entire computational domain is assumed to be symmetrical about the x-z plane that can save the computational cost. The constant-strength flat panel discretisation by boundary element method on the whole computational domain is shown

in Fig. 3. From the Fig. 3, we only distribute the panels on the step bottom without the sea bottom at deep depth h_1.

Fig. 4 (a) shows the wave patterns by a moving single source point of unit source density. The analytical solution of the linear steady-state wave patterns by Peters (1949) is used to validate the present calculations. Generally, with careful numeric, this type of Rankine source (or 'Simple-source', per Yeung (1982)) panel method provides good agreement with the analytical solutions. As the waves propagate to the far field downstream, a phase shift gradually appears; it is caused by the numerical dispersion and dissipation of the algorithm. A comparison between the waves in deep water and that in shallow water in Fig. 4 (b) and (c) shows that the wave length and amplitude are different.

Furthermore, the unsteady wave generated by Wigley hull would be simulated to calculate the wave-making resistance for validating the present algorithm. The dimensions of the Wigley hull model is shown in Table 1.

The simulation calculations for the case of a Wigley model is accelerated at $\dot{U} = 0.1g$ up to $F_n = 0.2$. The specific resistance R_ω/W is plotted as a function of the dimensionless time $t\sqrt{g/L}$, in which W is the weight of the model, and L is the model length. In the forced motion simulation, the ship is started impulsively from rest on a calm free surface. The curves of the calculated wave drag are shown in Fig. 5 and compared with the measured and calculated results. A case study on Wigley hull moving at $F_n = 0.2$ is conducted. Fig. 5 shows that a relatively better agreement than the steady wave resistance is achieved from the experiment measurements (Kajitani et al., 1983). The figure indicates that this case has a vertical shift between the present and calculation by Doctors et al. (2008). This finding is expected because nonlinear theory could provide a more accurate prediction than linear theory. Nevertheless, the frequency, phasing, and decaying of the oscillations appear to match effectively. The decaying oscillations indicate that the far-field condition in equation Eq. (6) can be satisfied without any reflection of the wave generated by the ship.

The convergence of the unsteady wave resistance is computed with different discretisation of the mesh on free surface; the fine mesh $N_x \times N_y = 80 \times 25$, standard mesh $N_x \times N_y = 100 \times 25$ and coarse mesh $N_x \times N_y = 120 \times 30$, where $N_x \times N_y$ represents the panel number in the longitudinal and transversal directions on free water surface in only half the domain. The results shown in Fig. 6 indicate the convergent at the standard mesh.

The convergence study for time step Δt is carried out on the same Wigley III hulls that start from rest. We calculate the wave resistance to examine the convergence of the present algorithm with different time steps (Δt). The panel size to ship length ratio at each Froude number is fixed at $\Delta x/L = 1/\kappa$. Then, the time can be non-dimensionalised by the following:

$$t' = \Delta x \bigg/ U = \frac{1}{\kappa F_n} \sqrt{\frac{L}{g}} \qquad (21)$$

In the present study, $\kappa = 60$. The results shown in Fig. 7 confirm the time step $\Delta t = 2t'$ used in the following simulations.

The time histories of wave resistance acting on Wigley hull with different tank width w/L are computed. We devote the following results in Fig. 8 to illustrate the importance of the physical dimensions of the towing tank on the expected unsteady effects on the wave resistance. The figure shows a strong influence of tank width for these unsteady calculations. When the dimensionless tank width $w/L = 1.0$, the rank walls play a negligible role at this test.

Using the scaled factor 8π adopted in the analysis method, the oscillation period T of the curves is a significant factor in the problem of the unsteady waves induced by the impulsive start or the uneven bottom. Consistent with the analytical result, the nondimensional period is defined as $T_e = Tg/8\pi U$ in Fig. 9. The $T_{e(2D)} \approx 1$ (when the transverse length across the y-axis is infinite). In the present 3D method, simulating
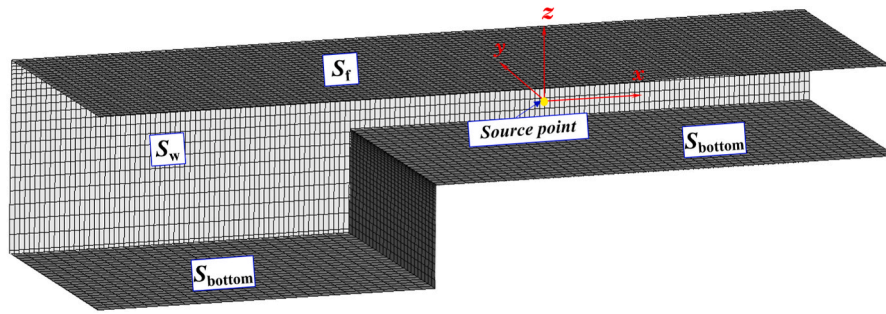
Fig. 3. Grid system of the source point and the whole computation domain for the simulation.
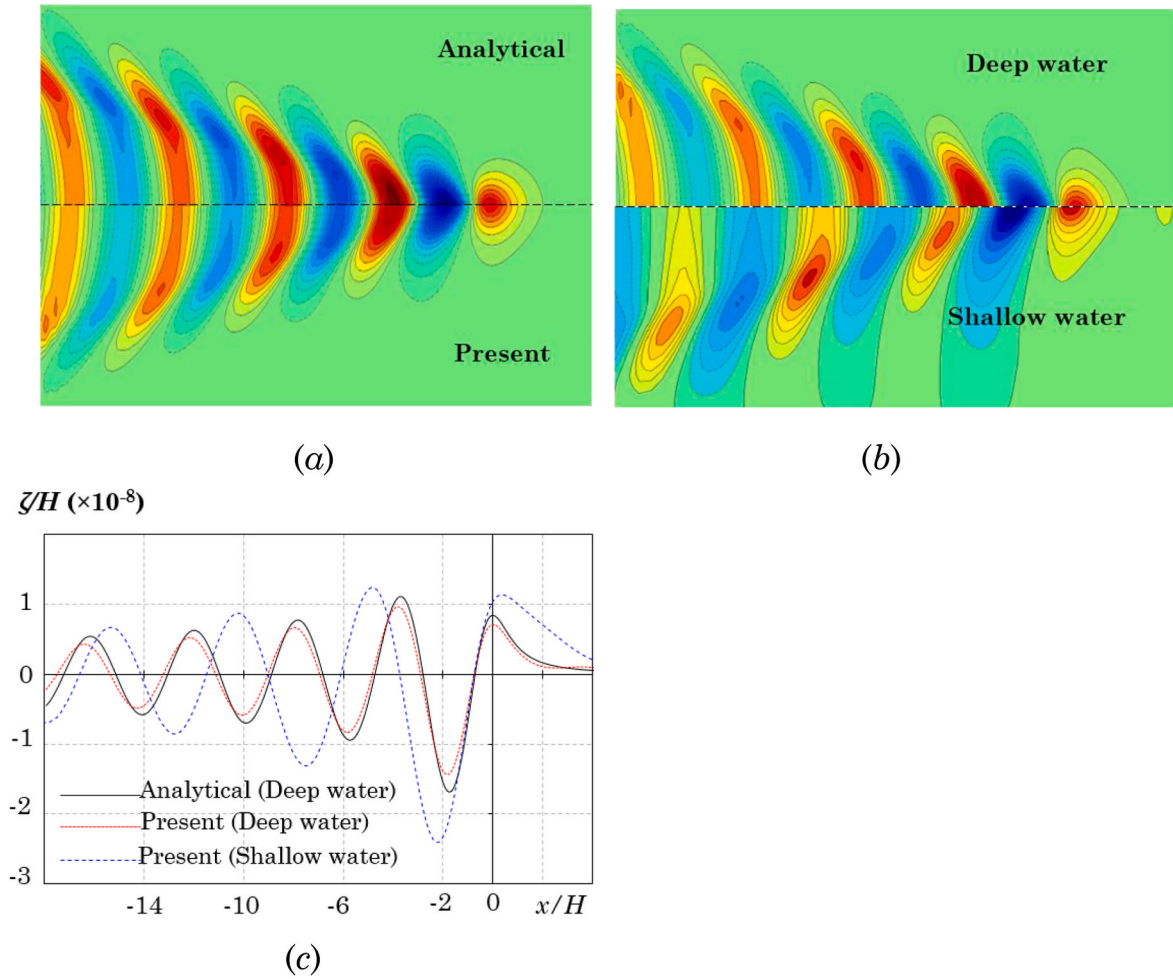

Fig. 4. Steady waves generated by a moving source point at $F_n = u/\sqrt{gH} = 0.8$ submerged at a depth of H, taken as $1/4$ steady wavelength, i.e., $H = 0.5\pi u^2/g$. (a) Comparison of deep water wave pattern between analytical solution and the present calculations. The horizontal and transverse axes are given by x/H and y/H, respectively. (b) Comparison of the wave patterns in deep water and shallow water (The water depth is $h = 1.05\ H$, and the depth Froude number is $F_h = 0.78$. (c) Comparison of the wave profile at the centreline: $y = 0$.

Table 1
Principal dimensions of the Wigley III model.

Dimension Item	Value
Length L (m)	3.0
Breadth B (m)	0.3
Draft D (m)	0.1875

the 'Quasi 2D' excitation on a 3D source is difficult due to the domain of the free-surface being limited. Therefore, the effect of the transverse length should be investigated. In that case, the T_e associated with different nondimensional width w/L of the sidewall would be predicted. In the present method, the results are compared with the theoretical analysis. Fig. 9 shows that the period T_e is in good agreement with the theoretical analysis when the transverse length w/L is 2.5 corresponding to $T_{e(2D)} \approx 1$.
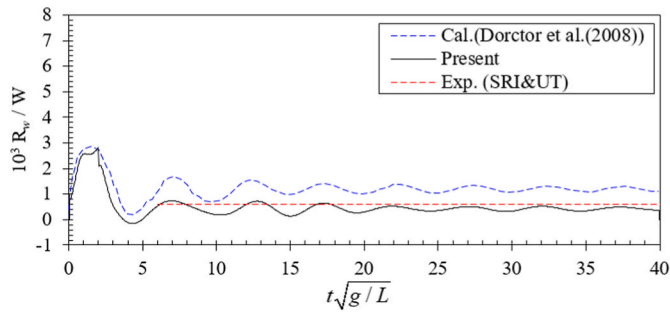
Fig. 5. Wave resistance coefficient at $F_n = 0.2$. The present results are compared with the simulation calculated by Doctors et al. (2008) based on linear theory and the experimental data from the steady tests conducted by the Ship Research Institution (SRI) and University of Tokyo (UT) (Kajitani et al., 1983).
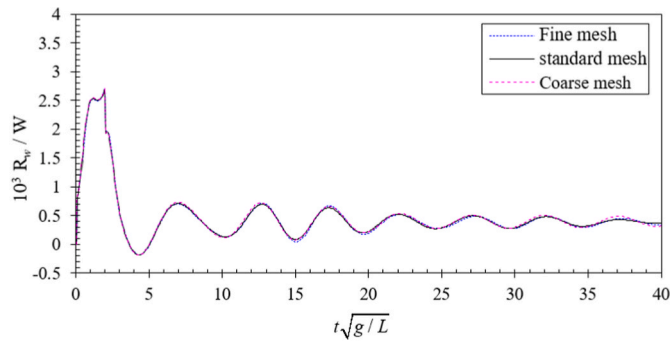

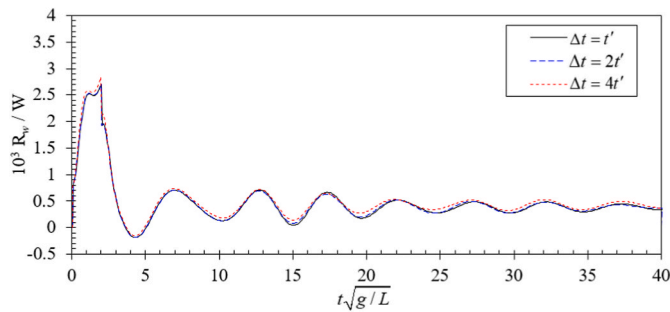**Fig. 6.** Convergence of the wave resistance coefficient R_ω / W at $F_n = 0.2$ varies with different mesh number.

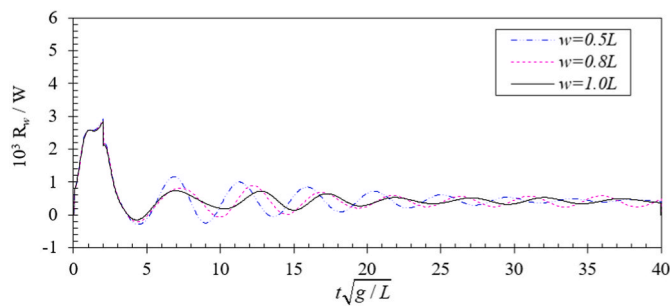**Fig. 7.** Convergence study on single Wigley hull starting from the rest to the constant speed $F_n = 0.2$.

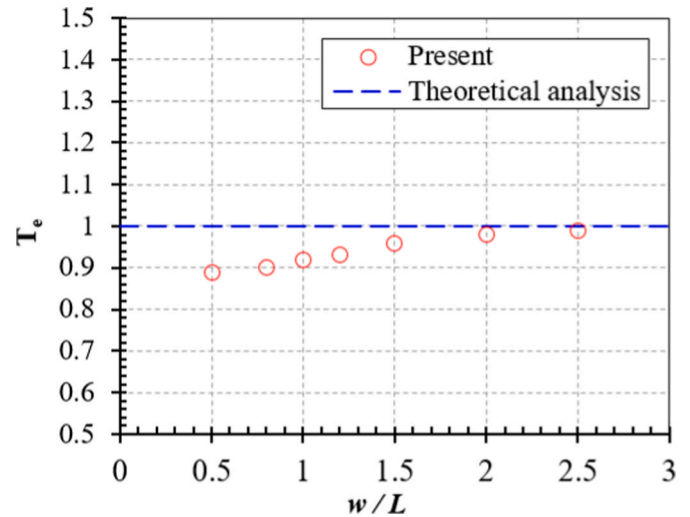**Fig. 8.** Wave resistance coefficient at $F_n = 0.2$ that varies with different tank widths w of the free surface.

Fig. 9. Comparison of the present period T_e with analytical approximation with different width w/L of the sidewall.

3.2. Results and discussions

Our implementation of the numerical algorithm has been validated by several test cases including flow over a single source and unsteady flow generated by an accelerating ship starting from rest. In this section, the present numerical method is extended to solve the problem of the unsteady wave generated by the ship over an uneven bottom. The computation results are compared with the results from the asymptotic analysis and numerical simulation based on linear theory by Grue (2017). The generation of mini-tsunami requires that the depth change, namely, $\Delta h = h_2 - h_1$ is comparable to the average water depth $h = (h_1 + h_2)/2$. When the depth change compares to the average water depth $\Delta h/h \simeq 1$, the mini-tsunami in observation emerges. The depth Froude number $F_h = U/\sqrt{gh}$ is in the range of 0.4–0.7, whereas the Froude number $F_n = U/\sqrt{gL}$ is in the range of 0.17–0.24. The cross-section of depth change adopts a smooth function, as follows:

$$z = -\frac{1}{2}\Delta h + \frac{1}{2}\Delta h \tanh(2d_l) \tag{22}$$

A uniform depth in the lateral direction is assumed in the simulation. To validate the present methodology and numerical method on the model of a ship constantly passing upon a step-bottom, we calculated the wave-making resistance coefficients C_w and wave-cut profile ζ from the centreline of the ship model. The non-dimensional wave-making resistance coefficient C_w is defined as follows:

$$C_w = \frac{-F_1}{0.5\rho U^2 S_b} \tag{23}$$

where S_b is the area of the wet body surface, F_1 denotes the wave-making resistance, and ρ is the density of the water. The ship is used by Grue (2017) with the parameters shown in Table 2.

A slow variation in ship speed should be ensured to minimise the disturbance due to start-up. The velocity U of the moving body has a gentle ramp-up phase with $U = U_0 \sin(t/T_0)$ when $t \leq T_0$ and $T_0\sqrt{g/h} = 30$. The initial position of the ship is $d_l = -30h$ away from the position d_l

Table 2
Principal dimensions of the ship model.

Dimensions Item	Value
Length (m)	10.18
Breadth (m)	1.59
Draft (m)	1.31

= 0. The average depth is $h = 2.5$ m. The results match well with those from Grue (2017), although a small vertical shift is found. This may be caused by different treatment of free-surface boundary conditions (nonlinear condition is used in the present study, while the linear condition is used by Grue). In Fig. 10, compared with the CFD results, the present calculations show a lower wave elevation of the upstream wave due to the CFD code that considers the effect of the viscidity term, which increases the viscous pressure resistance. However, the comparison confirms that the present numerical method can simulate the generation of the upstream long waves due to the depth change.

The generation of the upstream wave during the interaction between the ship with the depth change at $F_h = 0.51$ is shown in Fig. 11 at different times $t\sqrt{g/L} = 35$, 40, and 61. When the ship reaches the depth change at $d_l = 0$, the time is $t\sqrt{g/L} = 32$. The propagation speed of the wave right ahead of the ship is approximately $\sqrt{g(h - \Delta h/2)}$ between the time $t\sqrt{g/L} = 40$ and 61. It is basically characterised as a hump in the straight forward motion. At time $t\sqrt{g/L} = 40$, the phase of 'after the step' begins as soon as the stern of the ship has cleared the step; the interaction between the depth transition and the step does not cease immediately. Compared with $t\sqrt{g/L} = 35$, in $t\sqrt{g/L} = 40$, the bow wave decreases and the depression pattern around the ship can be observed, as shown in Fig. 11, thereby explaining the decrease in wave resistance shown in Fig. 14 (c), corresponding to $d_l/h = 3$ and 8.2, respectively. The detailed mechanism of ship-induced tsunamis is qualitatively illustrated in Grue (2020) and Wang and Cheng (2021).

In investigating the wave field related to the different times in Fig. 11, three wave patterns are plotted in Fig. 12. The figure clearly shows that the main leading wave propagates forward, and it maintains the shape with the same wave elevation during the period. For the ship moving over the depth change in Fig. 12(a), a wave crest is observed to be enlarged in the bow area. Thus, the wave resistance has an increment. Until the time $t\sqrt{g/L} = 40$ in Fig. 12(b), the leading wave propagates forward, and the Kelvin wake that corresponds to the time $t\sqrt{g/L} = 35$ is transformed. These wakes are replaced by a train of transverse waves with a higher wave crest. The region of the wave trough around the ship is substantially larger. In Fig. 12(c), after the leading wave moves forward, the bow wave region and the wave trough around the middle of the ship decrease substantially. Moreover, the wave resistance has a reduction shown in Fig. 14 (c) corresponding to $d_l/h = 8.2$. In addition, the wave amplitude is damped as the wave propagates to the transverse and backward boundary, indicating that the far field condition
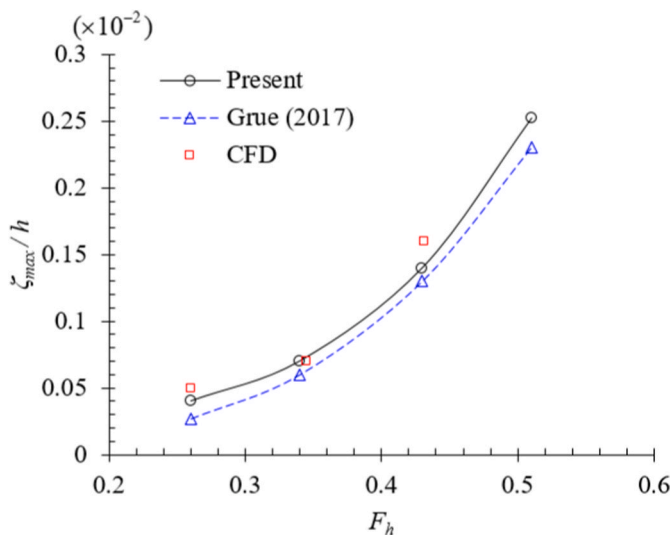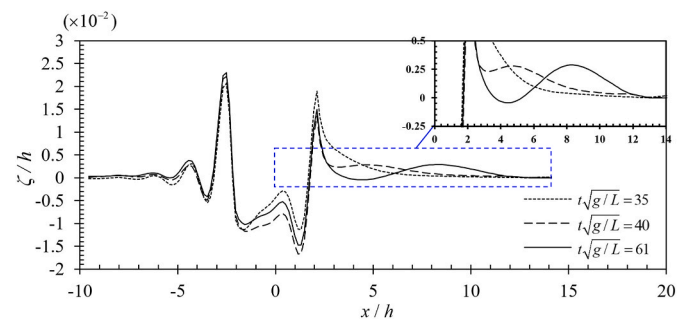

Fig. 11. Wave cuts of the upstream wave elevation ζ generated by ship after the depth change at $F_h = 0.51$ at different times $t\sqrt{g/L} = 35, 40, 61$. The origin of the ship reaches the centre position of depth change at $d_l = 0$ when $t\sqrt{g/L} = 32$.

implemented in the numerical method is reasonable. Finally, Fig. 12 confirms that the upstream wave was generated due to the effects of the interaction between the ship and the depth change. The numerical algorithm can supply an accurate prediction for the unsteady wave and wave resistance raised by the ship moving over depth change.

Fig. 13 shows the wave cuts of the upstream wave generated by the ship at different Froude number. The main upstream elevation clearly depends on the forward speed; the crest and trough of the leading wave increase with high F_h and very strong $\Delta h/h \simeq 1$. To qualify the effect of the interaction between the ship and the uneven bottom on the wave resistance, Fig. 14 shows the time history of the nondimensional wave resistance coefficient C_w acting on the ship when it passes over a step-like bottom. The obtained results are split into three different phases of the simulation as follows:

1. Acceleration and steady motion – this condition occurs before the ship reached the uneven bottom. The wave-field at this stage is developed during the period the ship starts from rest until its steady state; these discussions can be found in reference (Li et al., 2020a);
2. Transiting the step – the ship begins to interact with the uneven bottom. Initially, the wave resistance increases via the bow wave developed; it is partially compressed by the additional blockage, shown in Fig. 12(a). Then, whilst the step is located under the ship itself, the wave resistance coefficient C_w has a reduction and increases again, as shown in Fig. 12(b). This condition results from the interaction between the depth transition and the step on the stern of the ship.
3. After the step – once the ship has cleared the step and advanced about one ship length along the traveling way, the upstream wave propagates forward, as shown in Fig. 12(c). Correspondingly, the wave resistance C_w continuously reduces to a value lower than that of the steady value related to the first stage. Then, interestingly, the C_w starts to oscillate periodically around a mean steady resistance and persists for a long time before it decays to a steady-state value.

Fig. 14 shows that the waves will eventually approach those of the steady shallow-water waves when the transit time is sufficiently long. However, before the waves reach a new steady phase, they must experience a transition phase that is oscillatory in time. In the present work, we are interested in the upstream wave and the oscillating wave resistance C_w after the transition phase. The problem of how the deep water waves developed differently from the shallow water waves would be discussed. Therefore, Fig. 15 shows the time development of the wave cuts for the ship moving to pass the depth change at $F_h = 0.51$. During the first period around the $d_l/h = 0$–10 in Fig. 15, a small amplitude wave has been developed upstream, correspondingly, C_w has a reduction, which is shown in Fig. 14 (c). When the leading wave approaches the upstream boundary, it is damped due to the far field condition without any wave reflections. Subsequently, during each period, a train
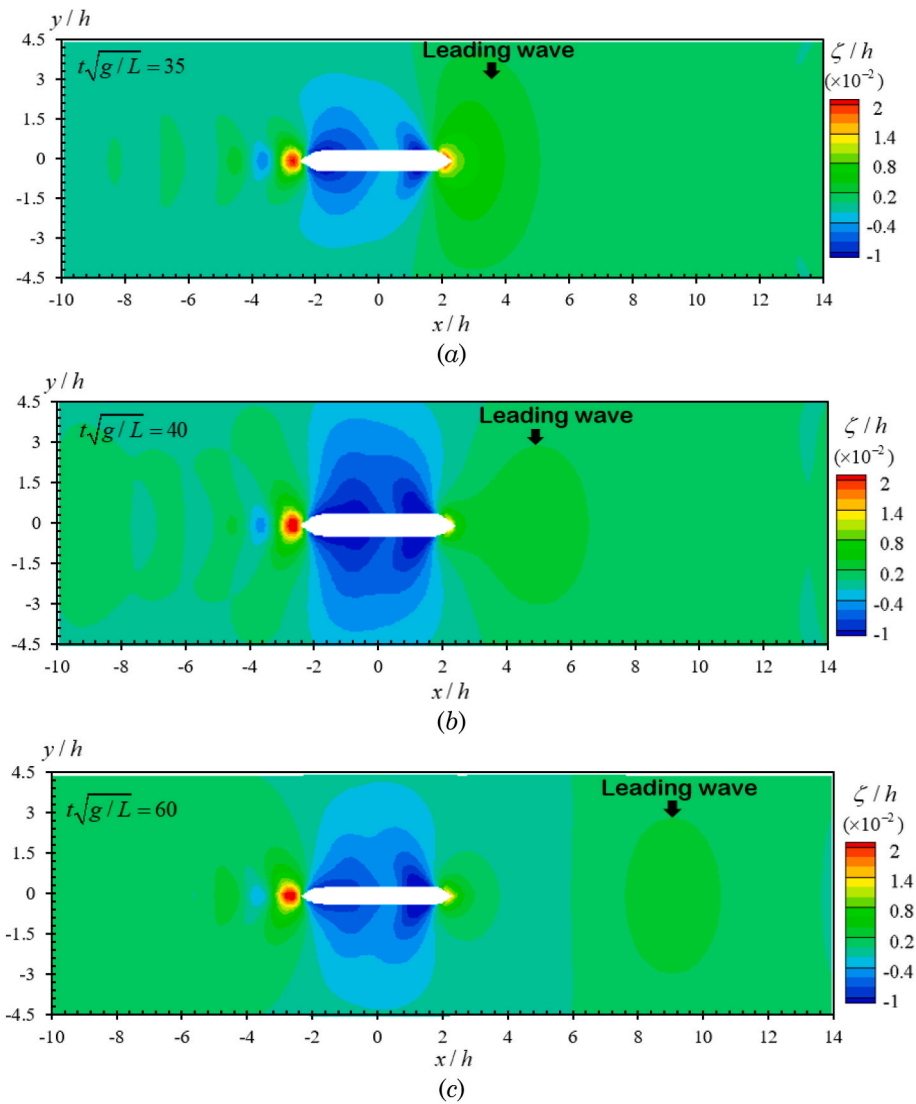

Fig. 10. Maximum upstream elevation ζ_{max} for ship moving from deep to shallow waters.

Fig. 12. Wave patterns of the upstream wave generated by ship at $F_h = 0.51$ at different time $t\sqrt{g/L} = 35, 40, 61$.
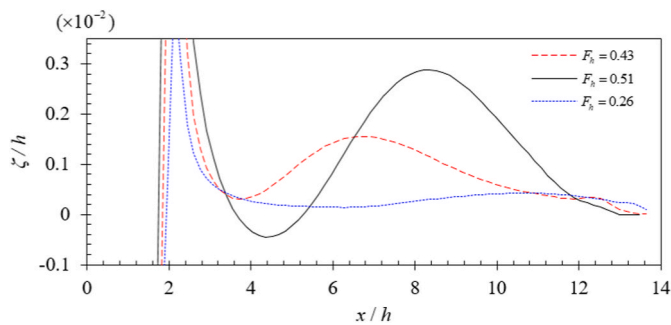

Fig. 13. Wave cuts of the upstream wave generated by ship at different F_h: $F_h = 0.26$, at $t\sqrt{g/L} = 45$; $F_h = 0.43$, at $t\sqrt{g/L} = 44$; $F_h = 0.51$, at $t\sqrt{g/L} = 60$.

of upstream waves propagates following the leading wave motion. The succeeding crests occur corresponding to each oscillation of the wave resistance.

Although we are mainly focused on the unsteady waves and the wave-making resistance when a ship is moving on a step bottom, it is of practical interest to investigate the ship squat and grounding problem. In the present modelling, the ship module is fixed, and the heave force (F_3)

and pitch moment (F_5) are calculated. The sinkage and trim can be simply calculated by dividing the force by the corresponding restoring coefficient K_3 and K_5. The results are shown in Fig. 16. A sudden increase of sinkage and trim is observed shortly after the ship crosses the step bottom. The peak values of the sinkage and trim are about two times of those in deep water. Then, the sinkage and trim will decrease quickly before reaching a periodical oscillation. This is very similar to the time history of the unsteady wave-making resistance. The fluctuation of wave-making resistance will result in speed-loss or speed-increase, while the fluctuations in sinkage and trim will result in squat and grounding. It requires special attention to adjust ship speed when it manoeuvres on a bottom with abrupt depth change.

4. Conclusions

In this article, we have presented a numerical simulation method based on the MEL to investigate the unsteady wash waves generated by the ship moving across a depth change. The study focuses on the upstream wave propagation and the oscillating wave resistance C_w at different Froude Numbers $F_h \sim 0.26–0.51$ and the $F_n \sim 0.17–0.24$. The nonlinear generation mechanism is numerically explored by the Rankine source method in the time domain valid for small $\Delta h/h$ and long waves. The impulsive force induced by the moving ship interacted with depth
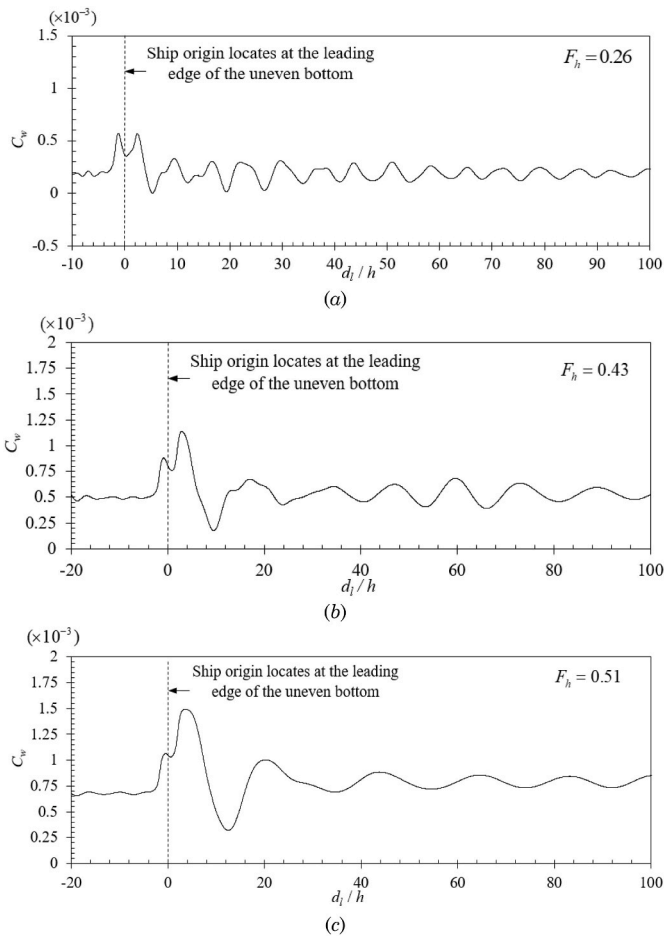
(a)

(b)

(c)

Fig. 14. Time histories of the nondimensional wave resistance C_w that varied with different F_h during whole numerical simulation with three stages. $d_l = 0$ corresponds to the instant when the ship origin reaches the leading edge of the step bottom.
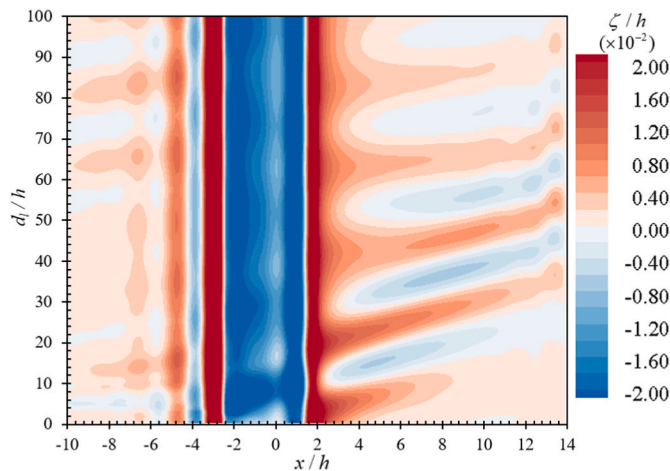

Fig. 15. Time development of wave cuts at the centreline of the ship model starts when the ship origin reaches the leading edge of the uneven bottom at $d_l = 0$. Results are shown for $F_h = 0.51$.

change providing an explanation of the upstream wave and the oscillating wave resistance. The upstream leading wave of elevation is formed by observations in the simulations. It could also result in a sharp increase in the vertical force acting on the ship. A train of slower waves
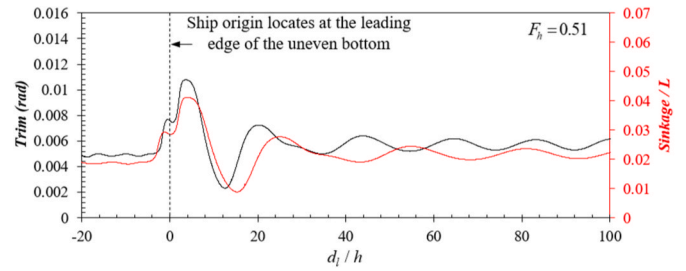

Fig. 16. Time histories of the sinkage and trim (Sinkage = F_3/K_3, and Trim = F_5/K_5) at $F_h = 0.51$. $dl = 0$ corresponds to the instant when the ship origin reaches the leading edge of the step bottom.

is formed and succeeded, causing the wave resistance amplitude to oscillate around the mean steady value. The forward speed has a pronounced effect on the leading wave height, where the upstream wave elevation grows according to F_h^n with n in the range 3–4. Finally, further study of the effects of the slope in the step-like bottom and the sidewall on the unsteady wash waves computed by the present method would be completed in the future.

CRediT authorship contribution statement

Mingxin Li: Conceptualization, Methodology, Software, Data curation, Writing – original draft. **Zhi-Ming Yuan:** Conceptualization, Writing – review & editing, Visualization, Supervision. **Longbin Tao:** Writing – review & editing, Investigation.

Declaration of competing interest

The authors declare that they have no known competing financial interests or personal relationships that could have appeared to influence the work reported in this paper.

Data availability

Data will be made available on request.

Acknowledgments

References

Alam, M.-R., Mei, C.C., 2008. Ships advancing near the critical speed in a shallow channel with a randomly uneven bed. J. Fluid Mech. 616, 397–417.

Beck, R.F., 1999a. Fully Nonlinear Water Wave Computations Using a Desigularized Euler-Lagrange Time-Domain Approach. University of Michigan, USA, Department of Naval Architecture and Marine Engineering, Ann Arbor, pp. 1–58. MI 48109-2145, Published in: Non-linear Water Wave Interaction, Advances in Fluid Mechanics Series, WIT Press.

Beck, R.F., 1999b. Fully Nonlinear Water Wave Computations Using a Desingularized Euler-Lagrange Time Domain Approach.

Bunnik, T.H.J., 1999. Seakeeping Calculations for Ships, Taking into Account the Non-linear Steady Waves. Ph.D. thesis. Delft University of Technology, The Netherlands.

Cao, Y., Beck, R.F., Schultz, W.W., 1993. Numerical computations of two-dimensional solitary waves generated by moving disturbances. Int. J. Numer. Methods Fluid. 17 (10), 905–920.

Chen, X.-N., Sharma, S.D., 1995. A slender ship moving at a near-critical speed in a shallow channel. J. Fluid Mech. 291, 263–285.

Cheng, Y., Xi, C., Dai, S., Ji, C., Collu, M., Li, M., Yuan, Z., Incecik, A., 2022. Wave energy extraction and hydroelastic response reduction of modular floating breakwaters as array wave energy converters integrated into a very large floating structure. Appl. Energy 306.

Dawson, C., 1977. A practical computer method for solving ship-wave problems. In: Proceedings of Second International Conference on Numerical Ship Hydrodynamics, pp. 30–38.

Doctors, L.J., Day, A.H., Clelland, D., 2008. Unsteady effects during resistance tests on a ship model in a towing tank. J. Ship Res. 52 (4), 263–273.

Dommermuth, D.G.Y., D, K.P., 1987. Numerical simulations of nonlinear axisymmetric flows with a free surface. Dommermuth, D.G. and D.K.P. Yue, 1987 J. Fluid Mech. 178, 195–219. ScienceDirect. Deep Sea Research Part B. Oceanographic Literature Review 34 (12), 1030.

Faltinsen, O.M., 1977. Numerical Solutions of Transient Nonlinear Free-Surface Motion outside or inside Moving Bodies.

Feng, D., Wang, X., Zhang, Z., Guan, Y., 2010. Time-domain nonlinear wave making simulation of the catamaran based on velocity potential boundary element method. In: International Conference on Offshore Mechanics and Arctic Engineering, pp. 621–628.

Gourlay, T., 2008. Slender-body methods for predicting ship squat. Ocean Eng. 35 (2), 191–200.

Grue, J., 2017. Ship generated mini-tsunamis. J. Fluid Mech. 816, 142–166.

Grue, J., 2020. Mini-Tsunami made by ship moving across a depth change. J. Waterw. Port, Coast. Ocean Eng. 146 (5), 04020023.

He, G., Kashiwagi, M., 2014. A time-domain higher-order boundary element method for 3D forward-speed radiation and diffraction problems. J.J.o.M.S., Technology 19 (2), 228–244.

Hess, J.L., Smith, A.M., 1964. Calculation of Non-lifting Potential Flow about Arbitrary Three-Dimensional Bodies. Douglas Aircraft Co Long Beach CA.

Jensen, G., 1986. Rankine Source Methods for Numerical Solutions of the Steady Wave Resistance Problems, 16th Symposium on Naval Hydrodynamics.

Jiang, T., Henn, R., Sharma, S.D., 2002. Wash waves generated by ships moving on fairways of varying topography. In: Taylor, R.D. (Ed.), Naval Hydrodynamics (Fukuoka, JAPAN).

Kajitani, H., Miyata, H., Ikehata, M., Tanaka, H., Adachi, H., Namimatsu, M., Ogiwara, S., 1983. The Summary of the Cooperative Experiment on Wigley Parabolic Model in Japan. Tokyo University.

Kara, F., Tang, C.Q., Vassalos, D., 2007. Time domain three-dimensional fully nonlinear computations of steady body–wave interaction problem. Ocean Eng. 34 (5/6), 776–789.

Kijima, K., Nakiri, Y., 1990. Prediction method of ship manoeuvrability in deep and shallow waters. In: Cross, C.S.J. (Ed.), Marine Simulation and Ship Manoeuvrability. C.S.J. Cross, Tokyo, Japan.

Kring, D.C., 1994. Time domain ship motions by a three-dimensional Rankine panel method. PhD Thesis 72–83.

Li, M.-X., Yuan, Z.-M., Tao, L., 2021. An iterative time-marching scheme for the investigation of hydrodynamic interaction between multi-ships during overtaking. J. Hydrodyn. 33 (3), 468–478.

Li, M., Yuan, Z.M., Yeung, R.W., 2020a. Unsteady Wave-Making Resistance of an Accelerating Ship, ASME 2020 39th International Conference on Ocean, Offshore and Arctic Engineering.

Li, M., Yuan, Z.M., Yeung, R.W., 2020b. Unsteady Waves Generated by a Ship Travelling over a Step Bottom, the 35th Intl Workshop on Water Waves and Floating Bodies (Seoul, Korea).

Li, Y., Sclavounos, P.D., 2002. Three-dimensional nonlinear solitary waves in shallow water generated by an advancing disturbance. J. Fluid Mech. 470, 383–410.

Longuet-Higgins, M.S., Cokelet, E.D., 1976. The Deformation of Steep Surface Waves on Water. I. A Numerical Method of Computation. Proceedings of the Royal Society A: Mathematical, Physical and Engineering Sciences.

Lunde, J.K., 1951. On the linearized theory of wave resistance for displacement ships in steady and accelerated motion. Trans. - Soc. Nav. Archit. Mar. Eng. 59, 25–76.

Nakos, D.E., Kring, D., Sclavounos, P.D., 1994. Rankine Panel Methods for Transient Free-Surface Flows.

Park, J.H., Troesch, A.W., 1993. Numerical modeling of short-time scale nonlinear water waves generated by large vertical motions of non-wallsided bodies. Phys. Rev. E 7 (1), 99–103.

Peters, A.S., 1949. A new treatment of the ship wave problem. Commun. Pure Appl. Math. 2 (2-3), 123–148.

Raven, H.C., 1996. A Solution Method for the Nonlinear Ship Wave Resistance Problem. PhD Thesis. Thèse Université technique de Delft.

Shi, W., Li, M., Yuan, Z., 2020. Investigation of the ship–seabed interaction with a high-fidelity CFD approach. J. Mar. Sci. Technol. 1–16.

Tang, C.Q., 2006. Time Domain Three-Dimensional Fully Nonlinear Computations for Body-Wave Interaction in a Dynamic Visualization Architecture. University of Strathclyde.

Terziev, M., Tezdogan, T., Incecik, A., 2020. Modelling the hydrodynamic effect of abrupt water depth changes on a ship travelling in restricted waters using CFD. Ships Offshore Struct. 1–17.

Torsvik, T., Dysthe, K., Pedersen, G., 2006. Influence of variable Froude number on waves generated by ships in shallow water. Phys. Fluids 18 (6), 062102.

Tuck, E.O., 1966. Shallow-water flows past slender bodies. J. Fluid Mech. 26 (1), 81–95.

Wang, P., Cheng, J., 2021. Mega-ship-generated tsunami: a field observation in tampa bay, Florida. J. Mar. Sci. Eng. 9 (437).

Wehausen, J.V., 1964. Effect of the initial acceleration upon the wave resistance of ship models. Journal of Ship Reaearch 7 (3), 38–50.

Yeung, R.W., 1978. On the interactions of slender ships in shallow water. J. Fluid Mech. 85 (1), 143–159.

Yeung, R.W., 1982. Numerical methods in free-surface flows. Annu. Rev. Fluid Mech. 14 (1), 395–442.

Yeung, R.W., Tan, W.T., 1980. Hydrodynamic interactions of ships with fixed obstacles. J. Ship Res. 24 (1).

Yuan, Z.M., Li, M.X., Ji, C.-Y., Li, L., Jia, L., Incecik, A., 2019. Steady hydrodynamic interaction between human swimmers. J. R. Soc. Interface 16 (150), 20180768.